Nanoscale Imaging with Resonant Coherent X Rays: Extension of Multiple-Wavelength Anomalous Diffraction to Nonperiodic Structures

A. Scherz,[1,*] D. Zhu,[1,2] R. Rick,[1,2] W. F. Schlotter,[3] S. Roy,[1,+] J. Lüning,[4] and J. Stöhr[1]

[1]*SSRL, Stanford Synchrotron Radiation Laboratory, 2575 Sand Hill Road, Menlo Park, California 94025, USA*
[2]*Department of Applied Physics, 316 Via Pueblo Mall, Stanford University, Stanford, California 94035-4090, USA*
[3]*Institut für Experimentalphysik, Universität Hamburg, Luruper Chaussee 149, 22761 Hamburg, Germany*
[4]*Laboratoire de Chimie Physique, Université Pierre et Marie Curie, UMR du CNRS (7614), 11 Rue Pierre et Marie Curie, 75005 Paris, France, and Synchrotron SOLEIL, BP 48 91192, Gif-sur-Yvette, France*

(Received 13 April 2008; published 13 August 2008)

The methodology of multiple-wavelength anomalous diffraction, widely used for macromolecular structure determination, is extended to the imaging of nonperiodic nanostructures. We demonstrate the solution of the phase problem by a combination of two resonantly recorded coherent scattering patterns at the carbon K edge (285 eV). Our approach merges iterative phase retrieval and x-ray holography approaches, yielding unique and rapid reconstructions. The element, chemical, and magnetic state specificity of our method further renders it widely applicable to a broad range of nanostructures, providing a spatial resolution that is limited, in principle, by wavelength only.

DOI: 10.1103/PhysRevLett.101.076101 PACS numbers: 68.37.Yz, 42.40.Kw, 61.05.cp

Multiple-wavelength anomalous diffraction (MAD) phasing has revolutionized macromolecular structure determination on atomic length scales and has become a well established technique in x-ray crystallography [1–4]. The intricacy of structure determination due to the lost phase information in diffraction measurements can be decreased to a manageable problem by labeling the unknown specimen with a few heavy atoms that serve as reference scatterers. From the known location of the reference atoms and resonantly tuning of the x-ray energy to change their contribution to the measured diffraction pattern, the phase problem can be solved. An important prerequisite for conventional MAD is the periodicity of the sample, achieved by assembly of biological molecules into a crystal.

Here we extend the methodology to noncrystalline specimens. We demonstrate our method by use of a nonperiodic assembly of polymer-based nano-objects and employ coherent soft x rays tuned to the carbon K absorption edge ($\sim$284 eV $\cong$ 4.4 nm). The phase problem is solved by combining scattering patterns of nearly the same wavelength which emphasize absorption and phase contrast, respectively. Our technique is broadly applicable to the study of nanostructures extending from organic systems to inorganic nanostructures and nanophases and may facilitate unique and accurate reconstruction of individual specimens by use of x-ray free electron lasers [5,6].

Our method builds on the concept of coherent x-ray scattering or lensless imaging which has been developed over the past decade to overcome lens limitations of x-ray microscopy. The resolution is fundamentally limited by the wavelength, only. It has been successfully demonstrated that the lost phase information can be recovered by computational phase retrieval algorithms, constituting a ''computational lens'' (CL) [7–10]. Another approach is Fourier transform holography, where the scattering pattern from the sample is encoded by a reference wave. The interference pattern can then be uniquely inverted into a real space image, but the resolution is limited by the size of the reference structure [11,12]. Our technique essentially merges the computational lens and holographic approaches. Tuning to atomic absorption resonances is a widely used synchrotron radiation method to obtain element specificity, and this method has also been used in conjunction with coherent scattering to obtain nanoscale images [12–15]. Here we use x-ray tunability not only for element specificity but, more importantly, as an interference technique for structure determination. We specifically utilize the strong change of the optical constants (OCs) or atomic scattering factors of matter across resonances at the threshold of core electron excitation energies. Similar to holography, this allows us to define a reference wave ψ_R emerging from part of the sample, which resonantly phases the nonresonantly scattered wave ψ_N from other parts of the sample. With this generalization of the reference, no prior information of the reference structure is required, and we record the energy dependence of the interference intensity

$$I(E) = |\psi_N + \psi_R(E)|^2 \quad (1)$$

across the resonance. The MAD imaging approach can be summarized as follows: Given the OCs of the resonant (R) material, the amplitudes of the two waves ψ_N and ψ_R and their respective phase difference are calculated in a first step from diffraction data recorded for at least two x-ray energies (in general, three energies are required). In a second step, the energy-independent MAD results serve as reciprocal space constraints to iteratively reconstruct the

R and non-R parts of the image. The additional constraints may be viewed as providing reference wave information. This allows a unique computational straightforward reconstruction of the object and distinguishes our technique from the standard CL approach. Since no additional apertures or focusing optics are required for phasing purposes, the sample region is fully accessible to sample manipulation tools, such as magnetic fields and optical beams.

A scanning electron micrograph (SEM) of the sample used in this proof of principle experiment is shown in Fig. 1. Polystyrene spheres, 300 and 90 nm in size, were dispersed from aqueous solution on a Si_3N_4 membrane. The 800 nm thick Au film prepared on the back side of the membrane by sputter deposition is opaque to soft x rays at the C K edge (attenuation length 34 nm). A round object hole was drilled through the Au film by a focused ion beam stopping at the silicon nitride membrane. This aperture confines the sample area to 1.2 μm in diameter and allows for a coherent illumination with x rays. In order to determine the OCs, a second macroscopic sample with 90 nm polystyrene spheres was prepared on a bare Si_3N_4 membrane, and its x-ray absorption spectrum was recorded in transmission.

The experiment was carried out on the soft x-ray coherent scattering beam line of the Stanford Synchrotron Radiation Laboratory (SSRL). The C K-edge absorption spectrum of the macroscopic sample was used to derive the imaginary part β of the refractive index. The real part δ was obtained by Kramers-Kronig conversion, using the measured absorption spectrum and normalizing it over an extended range to tabulated data (30 eV–30 keV) outside the resonance region [16]. Transversely coherent x rays were produced by spatial filtering the undulator source, while a monochromator imposed temporal coherence [13]. The energy resolving power $E/\Delta E > 5000$ of the spherical grating monochromator provided a longitudinal coherence length of at least $\xi_L > 4$ μm, while the transverse coherence length at the sample was $\xi_T > 5$ μm, assuring coherent illumination of the sample. The scattered intensity was recorded with an in-vacuum backside-illuminated CCD detector with thermoelectric cooling and 1300×1340 pixels of 20 μm width. The selected distance from the sample to the detector was 75 mm yielding a numerical aperture of NA $= 0.106$.

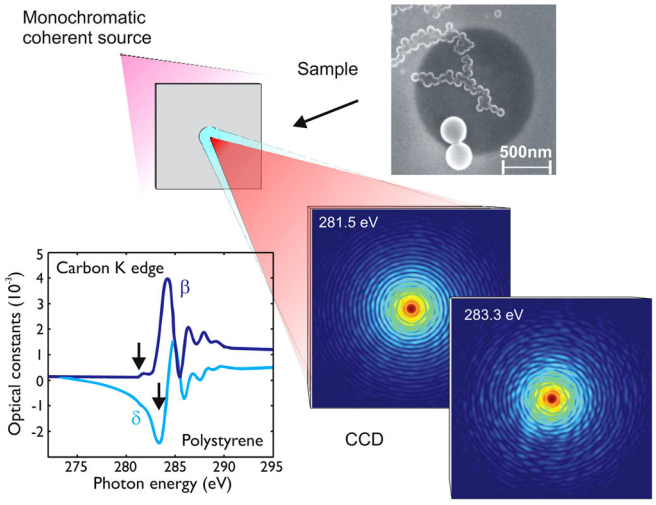

FIG. 1 (color online). Schematic experimental setup for MAD phasing: The sample (SEM image) is illuminated with a monochromatized and spatially coherent source (red). MAD phasing exploits the energy-dependent interference of the R exit wave (red) with the non-R exit wave (blue). The interference patterns recorded with a CCD detector reveal notable changes around the carbon K edge. The center portions of two intensity maps are shown on a logarithmic scale. The corresponding OCs for the selected energies are indicated in the plot.

In the far field of the sample, the scattered wave field reduces to the spatial Fourier transform $\mathcal{F}$ of the transmittance of the object. By assuming a weak R contrast of the object and linearizing the sample transmittance, we can decompose the exit wave into R and non-R contributions. The total scattered wave field is given by

$$\psi_{\mathrm{Tot}}(E, u, v) \propto \mathcal{F}[a_N(x, y) - (i\delta_E + \beta_E)a_R(x, y)], \quad (2)$$

where a_R and a_N represent the local arrangement of the R and non-R scatterers, respectively. The energy-dependent part is explicitly expressed by the OCs δ_E and β_E. Accordingly, a_R has real and positive values, and a_N is complex-valued. The intensity of the interference pattern across the resonance [Eq. (1)] is readily derived as

$$\begin{aligned} I(E) &\propto |A_N - (i\delta_E + \beta_E)A_R|^2 \\ &= |A_N|^2 + (\delta_E^2 + \beta_E^2)|A_R|^2 \\ &\quad - 2|A_N||A_R|(\delta_E \sin\Delta\phi + \beta_E \cos\Delta\phi), \end{aligned} \quad (3)$$

where $A_N(u, v)$ and $A_R(u, v)$ are the Fourier transforms of the spatial distribution of the scatterers a_R and a_N and $\Delta\phi(u, v) = \phi_N - \phi_R$ is their respective phase difference. Equation (3) forms the basis for resonant phasing used in MAD [4]. For each energy E_i, we obtain an independent interference pattern $I(E_i)$. From the knowledge of the optical constants, we can therefore determine the three unknown parameters $|A_N|$, $|A_R|$, and $\Delta\phi$ by collecting diffraction data at three different photon energies. Depending on the sample properties, one may take advantage of symmetry relations, as demonstrated in this work, and perform resonant phasing with two diffraction patterns, only.

In Fig. 1, we present the center portion of the two diffraction data recorded at 281.5 and 283.3 eV (wavelengths close to 4.4 nm) just before the absorption resonance. The high-q data were acquired using a movable round beam stop of 800 μm diameter, supported by a 14 μm thick wire. The exposure times were in the range of 700–1000 s with a coherent flux of $\sim 10^6$ photons s^{-1} $\mu\mathrm{m}^{-2}$. The low-q part extending to 0.009 nm^{-1} was recorded without the beam stop. A few pixels inside the Airy disk were thus affected by the direct

beam and were replaced by a fitted Airy disk, yielding almost undisturbed low-q diffraction data. The analysis included diffraction data with a maximum momentum transfer of $q_{\max} = 0.153$ nm^{-1} (800×800 pixels) limited by the signal-to-noise ratio. The interference pattern shows notable changes when the photon energy is varied depending on the R contrast mechanism. The pattern recorded at 283.3 eV exhibits odd centrosymmetric patterns which arise from phase contrast [13]. At 281.5 eV, the R amplitude decreases, and the non-R scattering from the circular aperture becomes prominent, leading to a more even centrosymmetric pattern. Given the realness of $a_R(x, y)$, we have, in general, the symmetry relations for the Fourier transform $A_R(u, v) = A_R^*(-u, -v)$. Because of the circular aperture, we have, in addition, the relation $A_N(u, v) = A_N(-u, -v)$. Consequently, we can rephrase the MAD equation (3) in terms of even and odd centrosymmetric parts gaining an additional condition for the solution:

$$I_{\text{sym}}(E) = |A_N|^2 - 2\beta_E |A_N||A_R| \cos\Delta\phi,$$
$$I_{\text{asym}}(E) = -2\delta_E |A_N||A_R| \sin\Delta\phi, \tag{4}$$

where we neglect higher order terms of the OCs in order to derive analytical solutions for the three unknown parameters from a minimum of two interference patterns.

The analytical and energy-independent MAD phasing results are shown in Fig. 2. The non-R amplitude reproduces, as expected, an Airy pattern from the circular aperture. In contrast, the R part shows a speckle pattern from the local arrangement of the polystyrene spheres. The nodes in the circular fringe pattern lead to pixels where amplitudes are not sampled because $|A_N| = 0$. As a result, faint circular shapes are also visible in the R part. Finally, the calculated phase relation $\Delta\phi$ is shown at the bottom. The gradual change of the phases covering the full range of angles without abrupt jumps indicates a stable and reliable determination of the phase pattern up to 0.153 nm^{-1}. The latter holds the key for recovering the object and determines the ultimate image resolution. If one knows the amplitude and phase of either the non-R or the R part, the object structure can be directly calculated by Fourier inversion. In practice, this will typically not be the case. Therefore, the phases ϕ_R and ϕ_N are disentangled iteratively. Since the two exit waves are related by $\Delta\phi$ (reciprocal space constraints) and originate from the same finite sample region (real space constraints), we have enough information to uniquely solve the problem. The developed reference-guided phase retrieval (RPR) algorithm is illustrated in Fig. 3. This new type of algorithm goes back and forth between the R and non-R amplitudes by applying the reciprocal space constraints $\Delta\phi$, with the phases ϕ_R and ϕ_N being iteratively updated. We used the simplest iterative algorithm, the error reduction method [7], to compute the phases. In principle, RPR is not limited to one specific iterative algorithm but can be easily combined with more sophisticated phase retrieval methods for advanced applications [7,9]. The real space constraints (support region) were derived from running the RPR with a loose support deduced from the autocorrelation of the Airy pattern. The reconstruction of the aperture was then taken to refine the support region.

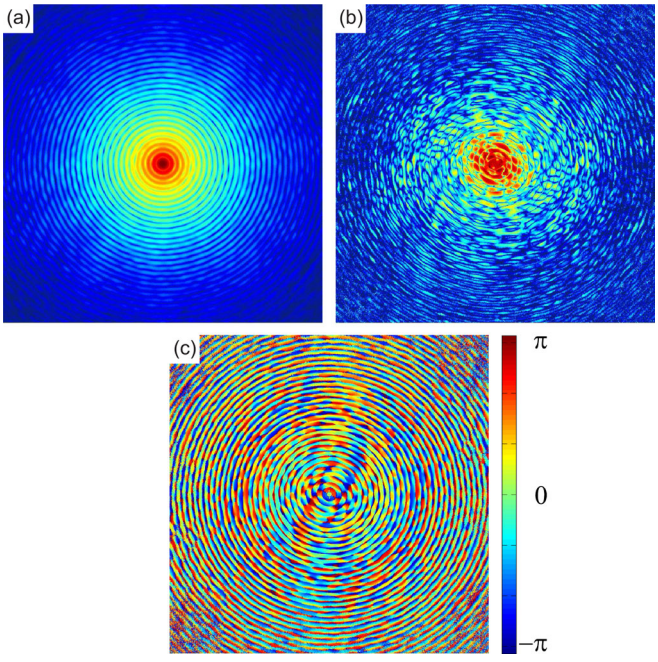

FIG. 2 (color online). MAD phasing results: (a) the amplitudes $|A_N|$ and (b) $|A_R|$. Intensities are shown on the same logarithmic scale. (c) The phase relation $\Delta\phi$ is obtained from the interference of the two components. 800×800 pixels are shown corresponding to 0.153 nm^{-1}.

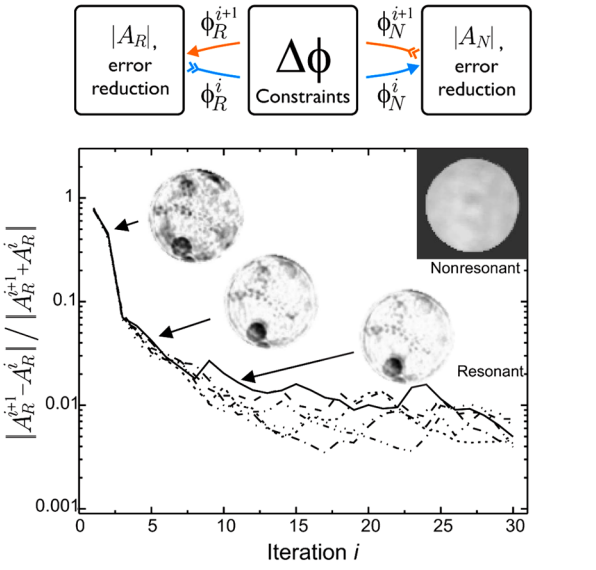

FIG. 3 (color online). Top: The diagram represents the iterative RPR method implementing the MAD phases $\Delta\phi$ as reciprocal space constraints between the R and non-R amplitudes. Bottom: The normalized convergence error is plotted against the iteration for a set of reconstructions with varying OCs. The insets show the progressing R structure determination and the non-R part (circular aperture).

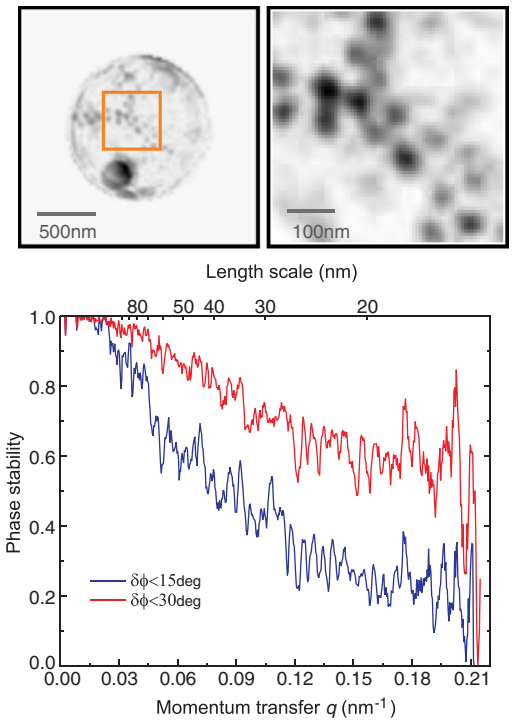

FIG. 4 (color online). (Top left) The final R structure of the polystyrene spheres and (top right) a magnified portion with adjusted linear contrast is presented. The 90 nm spheres are clearly resolved. The phase stability (bottom) suggests that image resolution is not better than 25 nm limited by the statistics at higher q.

The normalized convergence error [10] as a function of iteration is shown in Fig. 3 together with the progressive image reconstruction of the polystyrene spheres. After two iterations, the sample structure becomes apparent, consolidates over the next couple of iterations, and refines in less than 30 iterations. Simultaneously, the (non-R) aperture is being reconstructed. The groups of convergence curves represent different reconstructions, based on starting conditions with changes in the optical constants by 20%. The respective reconstructions are similar within 4% indicating the robustness of the RPR against uncertainties in the determination of OCs. We compared the MAD approach with the CL approach by applying the hybrid input-output (HIO) algorithm [7] to the diffraction pattern recorded at 283.3 eV using the same support region and knowing the sign of the OCs for this energy. The reconstructions with $\sim$1% convergence errors substantially differed in terms of nonflat backgrounds obscuring smaller structures and the appearance of a twin image of the spheres due to the high symmetry of the aperture. Other constraints need to be defined to possibly guide the HIO algorithm to the correct solution. The RPR method, on the other hand, yields unique and almost instantaneous reconstructions constituting only a fraction of the time it takes to record the data. We obtained individual images of the R spheres and the non-R circular aperture on the Si_3N_4 membrane. The final image of the polystyrene spheres in Fig. 4 is the average over 20 iterations from a single reconstruction after the convergence error leveled off at $<1\%$. Because of the full penetration of x rays through the polystyrene spheres, their thickness profile is revealed, and the intensity ratio 3:1 of the 300 nm sphere to the 90 nm ones is well reproduced. A magnification of the center area with adjusted linear contrast (top right) shows that the individual spheres vary consistently in intensity and diameter. The image resolution is ultimately given by the observation of interference terms originating from the R and non-R components. The phase pattern in Fig. 2 indicates that MAD phasing was sufficient up to 0.153 nm^{-1} corresponding to 21 nm. We further investigated the variance of the phases $\delta\phi$ after convergence is reached, as shown in the lower half of Fig. 4. A phase stability of 1.0 means that all phases at a given q remain within $\delta\phi$. The phase stability decays and levels off at 25 nm, suggesting that information at larger q is limited by statistics and will not improve the image resolution.

In conclusion, our experiment extends the methodology of MAD phasing to nonperiodic nanoscale objects. The method allows reliable and rapid object reconstructions from a set of energy-dependent R scattering patterns. The inherent resonant aspect of the method allows its application to a variety of heterogeneous systems, consisting of regions of different atomic constituents, chemical composition such as organic functional groups, and magnetic behavior such as changes in moments and their orientation.

The experiments were carried out at SSRL. Both SSRL and the conducted research are supported by the U.S. Department of Energy, Office of Basic Energy Sciences.

*Corresponding author.
scherz@slac.stanford.edu
+Present address: Advanced Light Source, Lawrence Berkeley National Laboratory, Berkeley, CA 94720, USA.

[1] Y. Okaya and R. Pepinsky, Phys. Rev. **103**, 1645 (1956).
[2] J. C. Phillips and K. O. Hodgson, Acta Crystallogr. Sect. A **36**, 856 (1980).
[3] J. M. Guss *et al.*, Science **241**, 806 (1988).
[4] W. A. Hendrickson, Science **254**, 51 (1991).
[5] R. Neutze *et al.*, Nature (London) **406**, 752 (2000).
[6] H. N. Chapman *et al.*, Nature (London) **448**, 676 (2007).
[7] J. R. Fienup, J. Opt. Soc. Am. A **4**, 118 (1987).
[8] J. Miao *et al.*, Nature (London) **400**, 342 (1999).
[9] S. Marchesini *et al.*, Phys. Rev. B **68**, 140101(R) (2003).
[10] P. Thibault *et al.*, Acta Crystallogr. Sect. A **62**, 248 (2006).
[11] I. McNulty *et al.*, Science **256**, 1009 (1992).
[12] S. Eisebitt *et al.*, Nature (London) **432**, 885 (2004).
[13] A. Scherz *et al.*, Phys. Rev. B **76**, 214410 (2007).
[14] T. Hauet *et al.*, Phys. Rev. B **77**, 184421 (2008).
[15] C. Song *et al.*, Phys. Rev. Lett. **100**, 025504 (2008).
[16] B. L. Henke *et al.*, At. Data Nucl. Data Tables **54**, 181 (1993).